ChemCatChem
Research Article
doi.org/10.1002/cctc.202401088
Chemistry Europe
European Chemical Societies Publishing
www.chemcatchem.org

$Ti_3C_2T_z$ Supported Pulse-Electrodeposited Pt Nanostructures for Enhanced Acidic Electrochemical Hydrogen Evolution

Sukanta Chakrabartty,[a] Haridas Parse,[a] Mathias Krämer,[b] Se-Ho Kim,[b, c] Dierk Raabe,[b] Baptiste Gault,[b, d] Maxim Sokol,[a] Brian A. Rosen,*[a] and Noam Eliaz*[a]

Platinum (Pt)-based electrocatalysts are considered benchmark materials for the hydrogen evolution reaction (HER) in acidic solution. However, widespread use is limited by the high price of Pt. Tuning the Pt morphology to increase the catalytic surface area for the same mass loading is therefore essential to increase its utilization. Herein, single $Ti_3C_2T_z$ flakes were deposited by electrophoresis onto a carbon-fiber gas diffusion layer, after which Pt nanostructures were selectively deposited onto the $Ti_3C_2T_z$ flakes by pulse electrodeposition. It was observed that the pulse on-time (t_{on}) and duration had a significant effect on the morphology and activity of the composite electrode towards HER. Flower-like and spherical morphologies were produced at long and short values of t_{on}, respectively. As-synthesized electrocatalysts were studied for HER in 0.5 M sulfuric acid (H_2SO_4). The catalyst with the lowest Pt loading (10 μg/cm^2), exhibited outstanding HER performance. It attained a current density of 10 mA/cm^2 at an overpotential of 38 mV, close to that of commercial carbon supported platinum (Pt/C, Vulcan XC). This catalyst exhibited a high turnover frequency (23.9 H_2 s^{-1} @ 100 mV), small Tafel slope (41 mV/dec), and high mass-specific activity (2.45 A/mg$_{Pt}$ @ 100 mV).

Introduction

The growing demand for energy and negative impact of fossil fuel utilization requires an efficient and environment friendly energy source.[1] Recently, hydrogen (H_2) has received enormous attention as a promising alternative to conventional fossil fuels.[2] H_2 as an energy carrier has many advantages over fossil fuel owing to its high gravimetric energy density and does not pollute the environment upon conversion to electricity.[3,4] As a consequence, demand for H_2 is expected to grow in future.[5] Among different H_2 production technologies, water electrolysis has gained significant importance as it can produce so-called green H_2 in an environment-friendly way by using renewable energy sources.[6] For the half reaction at the cathode, i.e. the hydrogen evolution reaction (HER), Pt-based electrocatalysts are commonly used.[7] Modulating surface structure by tuning morphology and size has been found promising to increase HER activity, and thus reducing the material required to achieve the comparable performance.[8–14] For instance, improved HER performance was reported for hierarchical dendrite like-Pt[13] or a pine-shaped Pt nanoarray.[14] While Pt nanoparticles are abundantly used for industrial applications, they are susceptible to agglomeration after prolonged activity and cycling, which in turn degrades their catalytic activity and durability.[15] Anchoring Pt nanoparticles on suitable support material such as transition metal carbides are known to be beneficial for enhancing electrocatalytic activity.[16] Strong metal-support interaction owing to similar electronic d-band structure of transition metal carbides and Pt has been shown to lead to stable electrochemical performance even with low Pt content.[17,18]

MXenes are a class of two-dimensional transition metal carbides and nitrides, and gained significant interest as a support material in the field of electrocatalysis[19–25] owing to its high conductivity, high surface area, hydrophilicity, and electrochemical activity.[20,24,25] MXenes are synthesized by the selective etching of the A-layer in MAX phases, $M_{n+1}AX_n$, where M represents an early transition metal, A is a group 13 or 14 element, and X represents carbon or nitrogen. The stoichiometry of MXenes is represented as $M_{n+1}X_nT_z$, where T_z stands for the surface termination group (typically -O, -OH, or -F). Recent literature reports revealed promising HER performance of MXene-Pt composites with low Pt content.[26–30] For instance, Yuan et al.[26] synthesized Pt nanoparticles (1.2 wt %) on $Ti_3C_2T_z$ by wet-impregnation and photo-induced methods and showed a small HER overpotential of 55 mV to reach 10 mA/cm^2. The high activity was attributed to electronic modification of Pt by the MXene. Another group deposited 3.0 wt % Pt on MXene by the atomic layer deposition technique.[27] Authors claimed excellent HER activity was due to uniform Pt dispersions on

---

[a] S. Chakrabartty, H. Parse, M. Sokol, B. A. Rosen, N. Eliaz
Department of Materials Science and Engineering, Tel Aviv University, Ramat Aviv 6997801, Israel
E-mail: barosen@post.tau.ac.il
neliaz@tauex.ac.il

[b] M. Krämer, S.-H. Kim, D. Raabe, B. Gault
Max Planck Institute for Sustainable Materials, Max-Plank-Straße 1, 240237 Düsseldorf, Germany

[c] S.-H. Kim
Department of Materials Science and Engineering, Korea University, Seoul 02841,Republic of Korea

[d] B. Gault
Department of Materials Science, Royal School of Mines, Imperial College, London London SW7 2AZ, United Kingdom

Supporting information for this article is available on the WWW under https://doi.org/10.1002/cctc.202401088

conductive MXene support. MXene provides strong metal-support interaction which could offer long-term stability by mitigating aggregation.[23] In this context, Zhang et al. synthesized highly stable single Pt atoms immobilized $Mo_2TiC_2T_z$ which had a mass activity 40 times higher than commercial Pt/C (Johnson Matthey) and could retain its HER performance up to 100 h.[28] The high stability is attributed to covalent bonding between Pt and $Mo_2TiC_2T_z$. In another approach, Li et al. synthesized Pt_3Ti intermetallic nanoparticle decorated $Ti_3C_2T_z$ by thermal reduction at 550 °C, that showed excellent HER catalytic activity with a small overpotential of 32.7 mV at 10 $mA\,cm^{-2}$.[29] Nevertheless, the electrochemical performance of Pt-based catalyst largely depends on the morphology, size, and distribution.[30] Synthesis methods which enables facile and easy preparation of Pt nanoparticles with desired morphology and size on MXene are therefore in high demand.

Electrodeposition is a promising technique and has many advantages over other available methods of synthesis. With this technique, the growth of the deposit particles can be easily controlled by adjusting parameters such as potential, current density, electrolyte, precursor concentration, and deposition time.[31–36] Furthermore, it is fast, efficient, reproducible, and demands a low energy input. As metal nanoparticles can be directly grown on the electrode/substrate, time consuming multi-steps including synthesis of catalyst requiring either high temperature or reducing agent and stabilizer can be readily avoided.

Despite several advantages, few reports are found in the literature which describe electrochemical deposition of Pt nanoparticles on MXene for HER.[37–41] Here, we first coated $Ti_3C_2T_z$ MXene by electrophoretic deposition (EPD) on a SIGRACET 29BC gas diffusion layer (hereafter, "GDL") like those used in electrolyzers, followed by selective electrodeposition of Pt onto the $Ti_3C_2T_z$. Different Pt morphologies were obtained by exploiting pulse electrodeposition, and HER performance was subsequently studied in acidic electrolyte as function of the electrodeposition conditions.

Experimental Section

Materials

Titanium (Ti, 99.7%), lithium fluoride (LiF, 99%), and aluminum (Al, 99.7%) powders were received from Strem (USA). Titanium carbide (TiC, 99.5%) and hexachloroplatinic acid ($H_2PtCl_6 \cdot 6H_2O$, $>$37.5% Pt basis) were obtained from Alfa Aesar (USA) and Merck (USA), respectively. Hydrochloric acid (HCl), sulfuric acid (H_2SO_4), were purchased from Lab-Chem. Commercial Vulcan XC–Pt (20 wt. % mass loading) and SIGRACET® 29BC gas diffusion layer carbon paper were purchased from Premetek (USA) and Ion-Power (USA), respectively. High purity deionized (DI) water was obtained using Milli-Q system (Millipore, USA).

Synthesis of MAX Ti_3AlC_2

The Ti_3AlC_2 MAX phase was synthesized using a reactive sintering route.[21] Briefly, TiC, Ti, and Al powders were mixed with a molar ratio of 2 : 1 : 1.05 and ball-milled at 1800 rpm for 5 min. The mixture was formed into a pellet and placed in an alumina crucible for annealing. The temperature of the furnace was kept at 1500 °C for 120 min. The heating rate was 5 °C/min. During annealing an inert atmosphere was maintained by flowing 200 sccm argon (Ar). Thereafter, the resulting sample was ball-milled to fine powder at 1800 rpm for 5 min.

Synthesis of MXene $Ti_3C_2T_z$

$Ti_3C_2T_z$ was synthesized from the Ti_3AlC_2 MAX phase following a modified LiF-HCl route.[21] Briefly, $Ti_3C_2T_z$ was obtained by selective etching of Al-layer of Ti_3AlC_2 using in-situ generated HF. Initially, LiF (0.5 g) was dissolved in 5 ml HCl (12 M) in a polyethylene vial. Later, Ti_3AlC_2 powder (0.5 g) was slowly added to the solution and stirred for 24 h at 35 °C. Post-etching, the slurry was washed with DI water repeated several times until an approximately neutral pH ($\geq$6) was reached. The washing step includes vigorous shaking followed by centrifugation at 5000 rpm for 5 min. After washing, the etched sediment was sonicated for 30 min in DI water in the presence of ice bath. The resulting black dispersion was then centrifuged at 5000 rpm for 30 min and the colloidal supernatant containing single layer of $Ti_3C_2T_z$ was collected. The $Ti_3C_2T_z$ colloid solution was purged with Ar and stored in a refrigerator to avoid oxidation. The yield was 7 mg/ml, obtained after drying the $Ti_3C_2T_z$ in a desiccator overnight.

Electrophoretic Deposition of $Ti_3C_2T_z$

EPD of $Ti_3C_2T_z$ was performed in a two-electrode cell. The carbon-fiber GDL and Pt-mesh were used as working and counter electrode, respectively. As GDL is hydrophobic, it was treated with water/ethanol (50 vol %) mixture before use. Freshly prepared $Ti_3C_2T_z$ solution was diluted by adding DI water and sonicated for 10 min. Diluted $Ti_3C_2T_z$ solution (1.5 mg/ml) was placed in the electrophoresis cell where GDL and Pt-mesh were immersed as electrodes at a distance of 1 cm. Deposition of $Ti_3C_2T_z$ was carried out by applying 5 V for 30 s using a Bio-Logic potentiostat.

Electrochemical Deposition of Pt

Electrodeposition of Pt was carried out using Bio-Logic potentiostat. Nitrogen purged solution containing 3 mM H_2PtCl_6 in 0.1 M KCl, which was used as the supporting electrolyte. The working electrode was the $Ti_3C_2T_z$@GDL described above while Pt-mesh and a saturated calomel electrode (SCE) were used as the counter and reference electrode, respectively. Direct current (DC) deposition of Pt was performed by holding potential at −0.42 V vs SCE for 600 s (hereafter denoted as MX_Pt-DC). All pulse experiments conducted in this study used a 50% duty cycle (θ). The potential during on-time (t_{on}) and off-time (t_{off}) was kept at −0.42 V vs. SCE and open circuit potential, respectively. The duration of t_{on} was 0.06, 3, and 15 s, corresponding to 10 k, 200, and 40 cycles, respectively, to keep the total t_{on} for each electrode fixed at 600 s. As-deposited catalysts were labelled as MX_Pt-0.06-10k, MX_Pt-3-200, and MX_Pt-15-40, respectively. Additionally, Pt was pulse electrodeposited with cycle number 5, where duration of t_{on} was 15 s (MX_Pt-15-5) in order to prepare a sample with low Pt loading.

Material Characterization

X-ray diffraction (XRD) measurements were performed using a Bruker D8 Discover diffractometer (Germany) with Cu–Kα (λ = 1.54 Å) radiation. XRD was taken on a GDL with an area of 1 cm^2. Scanning electron microscopy (SEM) analysis was acquired with

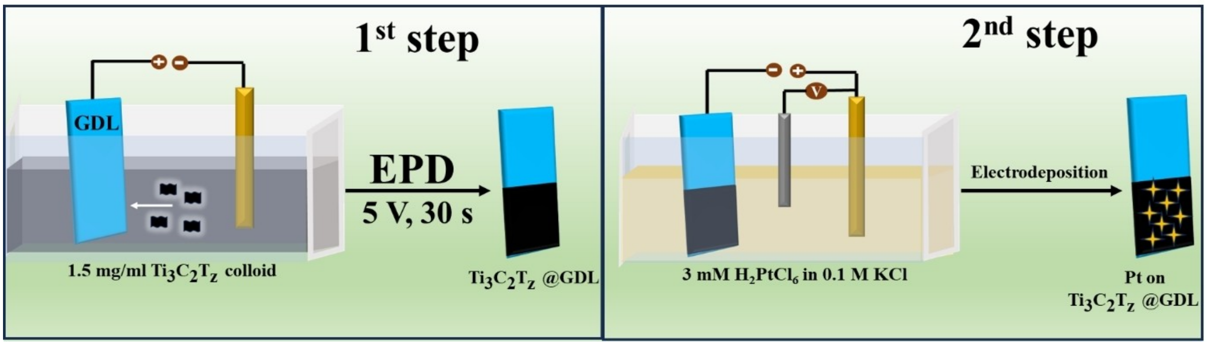

Figure 1. Schematic illustration of the electrophoretic deposition of $Ti_3C_2T_z$ on GDL and subsequent electrochemical deposition of Pt.

Quanta 200 FEG SEM coupled with an energy-dispersive X-ray spectroscopy (EDS) detector (X–Max SDD Oxford). Transmission electron microscopy (TEM), and high-resolution TEM (HRTEM), and selected area electron diffraction (SAED) analysis were performed using a Talos F200i (Thermo Scientific, USA). X-ray photoelectron spectroscopy (XPS) measurements were performed using the 5600 Multi-Technique System (PHI, USA) in ultra-high vacuum (2.5×10^{-10} Torr base pressure). The samples were irradiated with an Al–Kα monochromatic source (1486.6 eV) and the outgoing electrons were analyzed by a spherical capacitor analyzer using the slit aperture of 0.8 mm. XPS spectra were shifted to adventitious C1s peak at 284.8 eV. The contact angle measurement was done by using a tool made by Ramé-Hart instruments (USA). The measurement was done using a 2 μL DI water droplet at ambient temperature. The droplet was imaged by a magnified digital imaging setup providing the contact angle. The bulk composition of the samples was measured with inductively coupled-plasma mass spectrometry (ICP-MS, Perkin Elmer, USA).

Electrochemical Characterization

Electrochemical HER was performed with Bio-Logic potentiostat. The catalyst-coated GDL and graphite rod were used as working and counter electrodes, respectively. The working area of GDL was 0.2 cm^2. Ag/AgCl (sat. KCl) was used as the reference electrode. The electrolyte was 0.5 M H_2SO_4. The reference electrode's potential was converted to the reversible hydrogen electrode (RHE) using the following expression: $E_{RHE} = E_{AgCl} + E^0_{AgCl} + 0.059$ pH. Linear sweep voltammetry was obtained at scan rate of 5 mV/s. A stability test was performed by cyclic voltammetry (CV) and chronopotentiometry.

Results and Discussion

$Ti_3C_2T_z$-Pt nanostructures were synthesized in two steps as illustrated in Figure 1. $Ti_3C_2T_z$@GDL was first prepared by EPD of $Ti_3C_2T_z$ on GDL from its colloidal solution. $Ti_3C_2T_z$ flakes are net-negatively charged which is consistent with zeta potential measurements (Figure S1).

EPD was initiated by applying 5 V, resulting in the negatively charged $Ti_3C_2T_z$ flakes to migrate towards positively charged working electrode. This process yielded a uniform and thin film (0.32 μm) of $Ti_3C_2T_z$ (Figure S2). Subsequently, Pt nanostructures were directly grown on $Ti_3C_2T_z$ by pulse-electrodeposition. The Pt morphology and loading were controlled by changing t_{on} and cycle number using a constant duty cycle of 50 %.

The X-ray diffraction (XRD) was carried out to confirm the presence of $Ti_3C_2T_z$ and Pt nanostructures. Figure S3 shows that the characteristic (002) peak of Ti_3AlC_2 at $2\theta = 9.8°$ was broadened and shifted to a lower angle ($2\theta = 6.3°$) because of exfoliation, and the peaks (between 30 to 60°) corresponding to the MAX phase Ti_3AlC_2 nearly completely disappeared. Figure 2 shows the XRD profile of the $Ti_3C_2T_z$@GDL before and after the Pt electrodeposition step. Characteristic diffraction observed at 27.87°, 31.99°, 42.96°, and 57.2° correspond to the (001), (100), (101), and (110) planes of cubic Pt (JCPDS, No. 24–0771). Notably, the Pt diffraction intensity of MX_Pt-15-5 was weaker and broader than that of the other samples due to lower Pt content and smaller particle size. Also, the (002) peak of $Ti_3C_2T_z$ becomes indistinct after the electrodeposition of Pt. This could be due to spatial expansion of $Ti_3C_2T_z$ layers induced by the presence of Pt.[42]

The influence of t_{on} on the morphology of as-synthesized $Ti_3C_2T_z$-Pt nanostructures was analyzed by SEM shown in Figure 3. Quasi-spherical Pt particles with smooth surface were

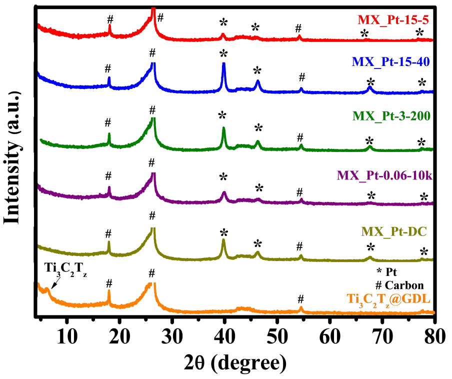

Figure 2. XRD profile of electrodeposited Pt nanostructures on $Ti_3C_2T_z$@GDL. The peak at 26° is from the carbon GDL and was cut to be able to show the MXene and Pt peaks.

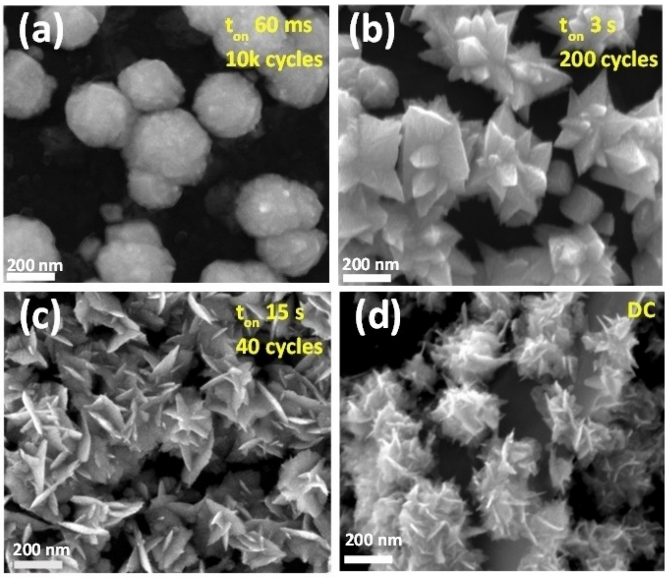

Figure 3. SEM images of (a) MX_Pt-0.06-10k, (b) MX_Pt-3-200, (c) MX_Pt-15-40, and (d) MX-Pt-DC.

obtained at a t_{on} of 0.06 s. When t_{on} increased to 3 s, a star-shaped Pt morphology was observed with sharp-edges. When t_{on} was further increased to 15 s, a flower-like morphology was obtained where sharp edges were maintained, but branches became flatter compared to the sample prepared using a 3 s t_{on}. Pt deposited by DC had a flower-like morphology with curved edges. This can be explained by the effect that pulsing has on the concentration profile of Pt near the growth front during electrodeposition. When t_{on} was small (0.06 s), the consumption of Pt ion was comparatively low and the lost Pt in the electrolyte adjacent to the growth front is quickly re-supplied by diffusion. As a result, the growth of elemental Pt takes place uniformly in all directions yielding smooth spherical morphology. As t_{on} is increased, the depletion of Pt from the deposition is not sufficiently replaced by diffusion and Pt crystals and mass transfer limitations cause the Pt to grow in an anisotropic manner owing to the non-uniform ternary current distribution, generating star ($t_{on}=3$ s) and flower-like ($t_{on}=15$ s) morphologies.

For comparison, direct current electrodeposition of Pt on GDL (i.e., without the $Ti_3C_2T_z$) yielded a significantly lower number of Pt particles (Figure S4). This is due to the hydrophobic nature of the microporous layer present in our GDL, as understood from contact angle measurement (Figure S5). By comparison, the hydrophilicity of $Ti_3C_2T_z$ maximizes the interaction area of the electrode with the electrolyte.[24]

After considering the effect of deposition parameters on the morphology of the Pt, the influence on the Pt content was studied. The Pt content of each electrode was measured quantitatively by ICP-MS analysis (Figure S6). Pt loading for MX_Pt-0.06-10k, MX_Pt-3-200, MX_Pt-15-40, MX_Pt-DC, and MX_Pt-15-5 was 134, 182, 188, 104, and 10 $\mu g/cm^2$, respectively. For context, the U.S. Department of Energy aims for water electrolyzer electrodes to have a max Pt loading of 125 $\mu g/cm^2$. MX_Pt-15-5 was selected for further characterization as it had the best mass-normalized activity towards HER, as will be discussed in the next section. MX_Pt-15-5 exhibited flower-like morphology as seen in SEM (Figure 4a), while both particle density and size decreased (Figure S7) by comparison to MX_Pt-15-40.

TEM imaging was consistent with SEM observation and further confirmed that flower-like Pt nanostructures are uni-

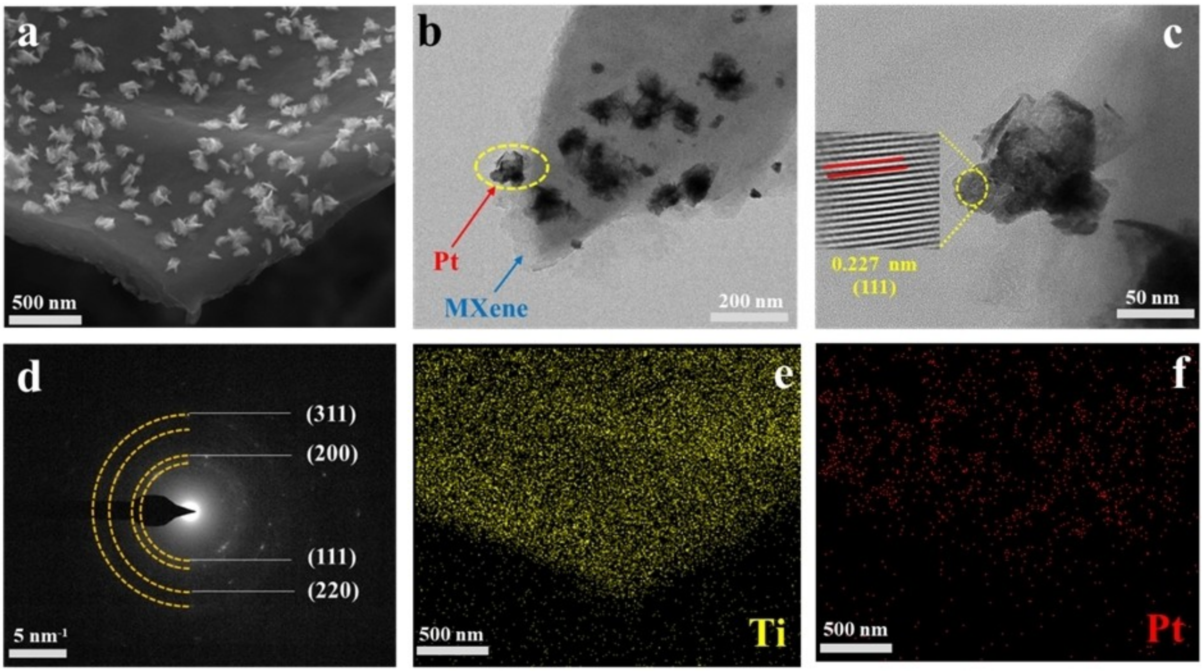

Figure 4. (a) SEM (b,c) TEM and HR-TEM images (d) SAED pattern of MX-Pt-15-5. SEM mapping analysis showing (e) Ti (f) Pt.

formly deposited over $Ti_3C_2T_z$ MXene (Figure 4b). The average size of the Pt nanostructures was 50 nm. Fringe-spacing (0.227 nm) obtained in HRTEM (Figure 4c) and selected angle electron diffraction (SAED) patterns (Figure 4d) correspond to Pt. Elemental mapping by EDS (Figure 4e,f) further confirm the homogeneous distribution of Pt on $Ti_3C_2T_z$.

The structure of surface chemical bonding was examined by XPS. The surface spectra comparison of $Ti_3C_2T_z$@GDL and MX_Pt-15-5 confirmed deposition of Pt (Figure 5a). The HR-XPS profile of Pt is shown in Figure 5b. Characteristic peaks centred at 71.0 eV and 73.4 eV, correspond to metallic Pt^0, while the other two peaks observed at 71.69 and 74.99 eV were attributed to Pt^{2+} (Pt–O).[41] In Figure 5c,d, the Ti 2p peaks of $Ti_3C_2T_z$@GDL and MX_Pt-15-5 consisted of three doublets which could be further deconvoluted into six peaks, corresponding to Ti–C, Ti–C-T_z, and Ti–O. The signature from Ti–C-T_z and Ti–O originated due to surface functionalization and surface oxidation, respectively.[41] The C1s profile (Figure 5e,f) shows the characteristic signature of Ti–C for $Ti_3C_2T_z$ @GDL and MX_Pt-15-5 at 282.2 and 282.07 eV, respectively.[43]

Electrochemical Characterization

The electrochemical surface area (ECSA) was calculated by integrating desorption peaks from hydrogen in the under-potential deposition region of the CV in 0.5 M H_2SO_4 (Figure S8). The ECSA increased with Pt loading as measured by ICP-OES except for the MX_Pt-0.06-10 k electrode which exhibited a significant drop in ECSA (0.56 m^2/g). On the other hand, the star-shaped (MX_Pt-3-200) and flower-like (MX_Pt-15-40, and MX_Pt-DC) electrocatalyst specimens exhibited comparatively higher ECSAs (4.9 and ~6 m^2/g). The larger ECSA values are likely associated with an increased in number of accessible Pt sites when taking on this morphology. Despite flower-like morphology, MX_Pt-15–5 possessed low ECSA due to its very low Pt loading.[44]

The influence of Pt morphology on HER was clearly visible in linear sweep voltammogram (Figure 6a). MX_Pt-15-5 had the highest current density when normalized by ECSA. This electrode required only 38 mV of overpotential to reach the 10 mA/cm^2 benchmark current density. By comparison, spherical Pt with smooth surfaces (MX_Pt-0.06-10 k) required 100 mV overpotential to reach the same current density. Moreover, the catalysts MX_Pt-15-40, MX_Pt-3-200, and MX_Pt-DC delivered 10 mA/cm^2 current density at an overpotential of 44, 53, and 81 mV, respectively. Measurements on pristine $Ti_3C_2T_z$ (i.e., without Pt) showed no significant HER activity; additionally, the activity of Pt deposited on the GDL without $Ti_3C_2T_z$ is inferior to that of MX_Pt-15-5 (Figure S9).

To better understand the HER kinetics and mechanism, the Tafel slope was evaluated using Tafel equation ($\eta = a + b \log j$), where b is the Tafel slope.[45] Elementary steps involved in acidic HER are Volmer, Tafel and Heyrovsky. Hydrogen evolution on an electrocatalyst surface can occur either through Volmer-Tafel or Volmer-Heyrovsky mechanism. Value of Tafel slope sheds light on possible HER mechanism and rate determining steps.[46] In this case, Tafel slope for MX_Pt-15-5 was calculated to be 41 mV/dec (Figure 6b), indicating that evolution of hydrogen proceeds through a Volmer-Heyrovsky pathway and electro-

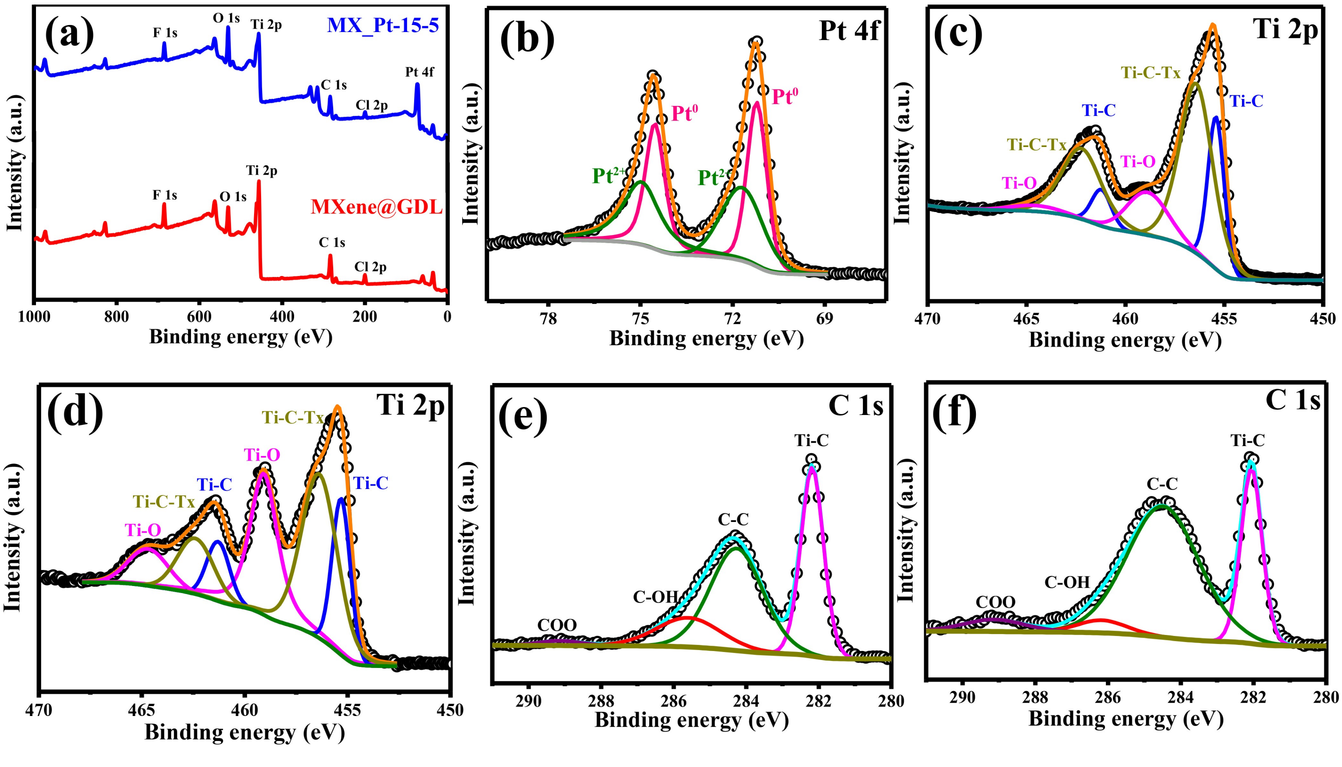

Figure 5. (a) Surface survey of MX_Pt-15-5 and $Ti_3C_2T_z$@GDL. (b)Deconvoluted XPS profiles of Pt 4f of MX_Pt-15-5. Deconvoluted XPS profiles of Ti 2p and C1s for (c,e) $Ti_3C_2T_z$ @GDL and (d.f) MX-Pt_15-5.

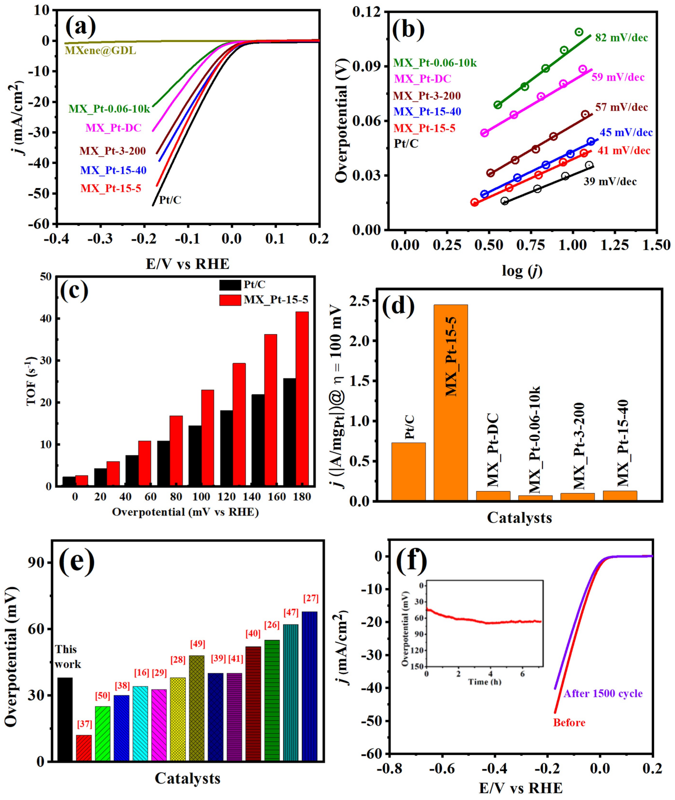

Figure 6. (a,b) Linear sweep voltammograms (5 mV/s) and the corresponding Tafel plot illustrating the HER activity of as-deposited catalysts (c) Plots illustrating the TOF of MX_Pt-15-5 and Pt/C. (d) Mass activity of as-deposited catalysts. (e) Comparison of overpotential @ 10 mA/cm^2 for MX_Pt-15-5 with other reported Pt@MXene catalysts. Bracketed numbers represent the reference from which the data point was taken (f) Voltammogram illustrates the durability of MX_Pt-15-5. Inset shows the change in potential with time.

chemical desorption step is the rate determining step. Furthermore, exchange current density (j_o) was measured by extrapolating the linear part of the Tafel slope (Figure S10). The exchange current density of MX_Pt-15-5 was 1.16 mA/cm^2 which was closer to that of commercial Pt/C (1.55 mA/cm^2). The low Tafel slope and high exchange current density implies faster charge transfer kinetics and high intrinsic HER activity of MX_Pt-15-5. Superior intrinsic activity of MX_Pt-15-5 was further confirmed from the calculated turnover frequency (TOF) (Figure 6c), i.e. the efficiency of the catalyst.[37] The TOF values for the MX_Pt-15–5 electrode were 23.9, 36.3, 42 H_2 s^{-1} at overpotentials of 100, 150, and 175 mV, respectively, considerably higher than that of commercial Pt/C (14.4, 22, 25 H_2 s^{-1}).

Furthermore, MX_Pt-15–5 outperformed commercial Pt/C in terms of mass activity (Figure 6d). The mass activity of MX_Pt-15-5 (2.45 A/mg$_{Pt}$ @ 100 mV) was 3 times larger than Pt/C (0.75 A/mg$_{Pt}$). The ECSA-specific activity of MX_Pt-15-5 was also higher than Pt/C (Figure S11). The high activity could be ascribed to the flower-like morphology of Pt promoting enhanced access of more catalytic sites and high-index planes. Figure 6e compares HER performance of MX_Pt-15-5 with previously reported MXene-Pt based electrocatalysts. Details can be found in supporting information Table S1.

In addition to electrocatalytic activity, evaluation of catalyst stability in harsh environment is also crucial. Durability of MX_Pt-15-5 was examined in acidic pH by cyclic voltammetry and chronopotentiometry. The MX_Pt-15-5 electrode was subjected to potential cycling between 0.07 V and −0.075 V vs RHE at 200 mV/s. Even after 1500 cycles, only 17 mV increase in overpotential is observed, suggesting good electrochemical stability (Figure 6f). By comparison, commercial Pt/C (Figure S12) and chemically deposited Pt@GDL (Figure S13) after the same potential cycling required an extra 80 and 65 mV of overpotential to reach same current density, respectively. The durability of MX_Pt-15-5 was further tested using chronoamperometry at a fixed current density of 10 mA/cm^2. Only a small (25 mV) increase in overpotential was observed after 7 h of HER (Figure 6f, inset).

Post-HER characterizations of MX_Pt-15-5 were performed using XRD and SEM to understand any phase and morphological change after durability test. Figure 7a compares the XRD pattern before and after the durability test. It is evident that the characteristic XRD signature of Pt was retained, and no additional peak was observed, implying structural stability of MX_Pt-15-5. Furthermore, no structural degradation of MX_Pt-

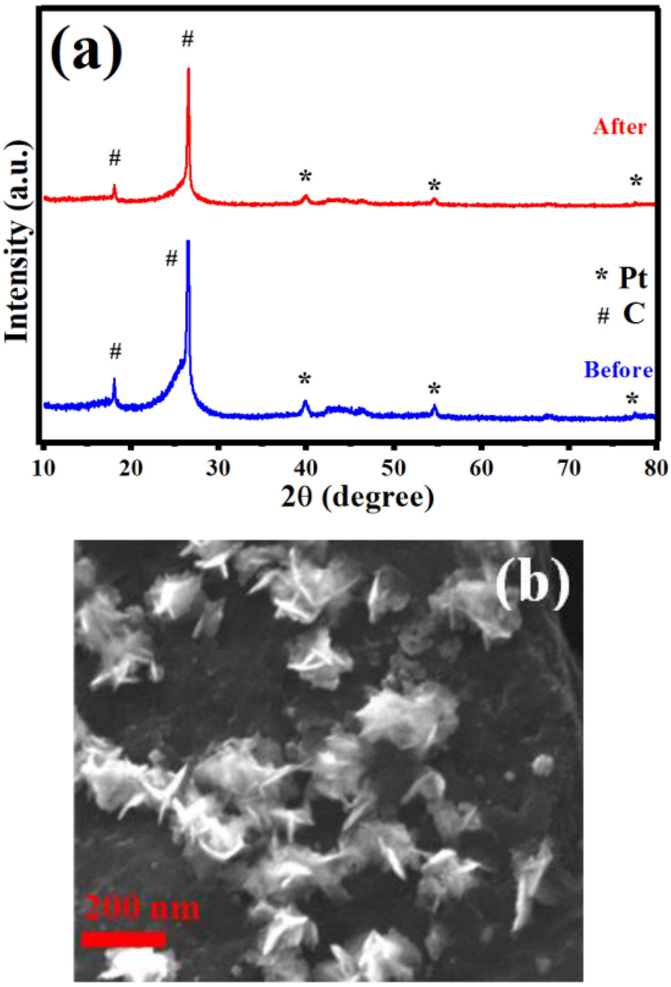

Figure 7. Post-HER XRD profile (a) and SEM image (b) of MX_Pt-15-5 after 7 h durability test.

15-5 was noticed in SEM images (Figure 7b). Post-HER SEM mapping (Figure S14) shows Pt nanostructures remained disperse uniformly without any agglomeration. Even though MX_ Pt-15–5 maintains phase and structural stability, its durability is not up to the mark. To shed light on this, post-HER XPS was performed. Figure S15 reveals the presence of higher oxidation state of Ti due to formation of amorphous Ti–O species which could be associated with HER performance loss.

Conclusions

Pt@$Ti_3C_2T_z$ electrocatalysts with low Pt loading were fabricated using electrophoresis of $Ti_3C_2T_z$ onto a GDL followed by pulse electrodeposition of Pt. The pulse on-time and cycle number controlled the Pt morphology and size by controlling the concentration of Pt adjacent to the electrode during the deposition process. MX_Pt-15-5 exhibited superior HER performance and outperformed commercial Pt/C in terms of turnover frequency and mass activity. The same electrode also performed favorably compared to commercial Pt@Vulcan XC in durability tests performed by potential cycling. Electrophoresis and electrodeposition may therefore be considered as valuable techniques towards the future design of electrolyzer electrodes containing MXene-support Pt nanoparticles.

Supporting Information Summary

Supporting information contains electrodeposition of Pt on GDL(Pt@GDL), calculation of electrochemically active surface area (ECSA), calculation of Turnover frequency (TOF), Zeta potential measurement of $Ti_3C_2T_z$, SEM image (cross section) of $Ti_3C_2T_z$@GDL, XRD profile of Ti_3AlC_2 and $Ti_3C_2T_z$, SEM image of Pt@GDL, contact angle measurement, Pt loading obtained from ICP-MS analysis, Average Pt size of electrocatalysts, ECSA of electrocatalysts, LSV of Pt@GDL, exchange current density (j_0) of MX_Pt-15-5 and Pt/C, ECSA specific activity of electrocatalysts, durability of Pt/C and Pt@GDL, post-durability SEM mapping, post-durability XPS profile of Ti, MX_Pt-15-5, and comparison table.

Acknowledgements

This work was financially supported by the Deutsche Forschungsgemeinschaft (DFG) DIP grant (EL869/1-1 RA 659/30-1).

Conflict of Interests

The authors declare no conflict of interest.

Data Availability Statement

The data that support the findings of this study are available in the supplementary material of this article.

Keywords: Pulse-electrodeposition · $Ti_3C_2T_z$-MXene · Pt · Hydrogen evolution reaction · Electrophoresis · Structure-activity

[1] J. Chow, R. J. Kopp, P. R. Portney, *Science.* **2003**, *302*, 1528–1531.
[2] M. S. Dresselhaus, I. L. Thomas, *Nature.* **2001**, *414*, 332–337.
[3] I. Staffell, D. Scamman, A. V. Abad, P. Balcombe, P. E. Dodds, P. Ekins, N. Shah, K. R. Ward, *Energy Environ. Sci.* **2019**, *12*, 463–491.
[4] M. A. Rosen, S. Koohi-Faye, *Energ. Ecol. Environ.* **2016**, *1*, 10–29.
[5] J. M. Ogden, *Phys. Today.* **2002**, *55*, 69–75.
[6] P. Nikolaidis, A. Poullikkas, *Renewable Sustainable Energy Rev.* **2017**, *67*, 597–611.
[7] R. J. Levie, *Electroanal. Chem.* **1999**, *476*, 92–93.
[8] Z. W. Seh, J. Kibsgaard, C. F. Dickens, I. Chorkendorff, J. K. Nørskov, T. F. Jaramillo, *Science.* **2017**, *355*, eaad4998.
[9] J. Chen, B. Lim, E. P. Lee, Y. Xia, *Nano Today* **2009**, *4*, 81–95.
[10] L. Lin, Z. Sun, M. Yuan, J. He, R. Long, H. Li, C. Nan, G. Sun, S. Ma, C. Chen, Y. J. Kang, Z. Y. Huo, Z. W. Zhu, W. Y. Huang, H. L. L. Xin, J. D. Snyder, D. G. Li, J. A. Herron, M. Mavrikakis, M. Chi, K. L. More, Y. Li, N. M. Markovic, G. A. Somorjai, P. Yang, V. R. Stamenkovic, *Science* **2014**, *343*, 1339–1343.
[11] Z. M. Cao, H. Q. Li, C. Y. Zhan, J. W. Zhang, W. Wang, B. B. Xu, F. Lu, Y. Q. Jiang, Z. X. Xie, L. S. Zheng, *Nanoscale.* **2018**, *10*, 5072–5077.
[12] T. L. Tan, L.-L. Wang, J. Zhang, D. D. Johnson, K. Bai, *ACS Catal.* **2015**, *5*, 2376–2383.
[13] L. Lin, Z. Sun, M. Yuan, J. He, R. Long, H. Li, C. Nan, G. Gun, S. J. Ma, *Mater. Chem.* **2018**, *6*, 8068–8077.
[14] Y. Li, H. Zhang, T. Xu, Z. Lu, X. Wu, P. Wan, X. Sun, L. Jiang, *Adv. Funct. Mater.* **2015**, *25*, 1737–1744.
[15] J. C. Meier, C. Galeano, I. Katsounaros, J. Witte, H. J. Bongard, A. A. Topalov, C. Baldizzone, S. Mezzavilla, F. Schüth, K. J. J. Mayrhofer, *Beilstein J. Nanotechnol.* **2014**, *5*, 44–67.
[16] Y. Wu, W. Wei, R. Yu, L. Xia, X. Hong, J. Zhu, J. Li, L. Lv, W. Chen, Y. Zhao, L. Zhou, L. Mai, *Adv. Funct. Mater.* **2022**, *32*, 2110910.
[17] D. V. Esposito, S. T. Hunt, Y. C. Kimmel, J. G. Chen, *J. Am. Chem. Soc.* **2012**, *134*, 3025–3033.
[18] Y. C. Kimmel, L. Yang, T. G. Kelly, S. A. Rykov, J. G. J. Chen, *Catal.* **2014**, *312*, 216–220.
[19] M. Naguib, V. N. Mochalin, M. W. Barsoum, Y. Gogotsi, *Adv. Mater.* **2014**, *26*, 992–1005.
[20] L. Verger, V. Natu, M. Carey, M. W. Barsoum, *Trends Chem.* **2019**, *1*, 656.
[21] B. Favelukis, S. Chakrabartty, V. Kumar, S.-H. Kim, A. El-Zoka, M. Krämer, D. Rabbe, G. Bault, N. Eliaz, A. Natan, M. Sokol, B. A. Rosen, *Adv. Funct. Mater.* **2024**, *34*, 2309749.
[22] Z. Kang, M. A. Khan, Y. Gong, R. Javed, Y. Xu, D. Ye, H. Zhao, J. Zhang, *J. Mater. Chem. A.* **2021**, *9*, 6089–6108.
[23] W. Kong, J. Deng, L. Li, *J. Mater. Chem. A.* **2022**, *10*, 14674.
[24] L. Yu, L. Lu, X. Zhou, L. Xu, *Adv. Mater. Interfaces.* **2022**, *10*, 2201818.
[25] A. Liu, X. Liang, X. Ren, W. Guan, M. Gao, Y. Yang, Q. Yang, L. Gao, Y. Li, T. Ma, *Adv. Funct. Mater.* **2020**, *30*, 2003437.
[26] Y. Yuan, H. Li, L. Wang, L. Zhang, D. Shi, Y. Hong, J. Sun, *ACS Sustainable Chem. Eng.* **2019**, *7*, 4266–4273.
[27] X. Zhang, B. Shao, S. Sun, Z. Gao, Y. Qin, C. Zhang, F. Cui, X. Yang, *Ind. Eng. Chem. Res.* **2020**, *59*, 1822–1828.
[28] J. Zhang, Y. Zhao, X. Guo, C. Chen, C.-L. Dong, R.-S. Liu, C.-P. Han, Y. Li, Y. Gogotsi, G. Wang, *Nat. Catal.* **2018**, *1*, 985.
[29] Z. Li, Z. Qi, S. Wang, T. Ma, L. Zhou, Z. Wu, X. Luan, F.-Y. Lin, M. Chen, J. T. Miller, H. Xin, W. Huang, Y. Wu, *Nano Lett.* **2019**, *19*, 5102–5108.
[30] B. Li, R. Ye, Q. Wang, X. Liu, P. Fang, J. Hu, *Ionics.* **2021**, *27*, 1221–1231.
[31] Y. Shi, C. Lee, X. Tan, L. Yang, Q. Zhu, X. Loh, J. Xu, Q. Yan, *Small Structures* **2022**, *3*, 2100185.
[32] B. A. Rosen, E. Gileadi, N. Eliaz, *J. Electroanal. Chem.* **2014**, *731*, 93–99.
[33] T. Nusbaum, B. A. Rosen, E. Gileadi, N. Eliaz, *J. Electrochem. Soc.* **2015**, *162* (7), D250–D255.
[34] E. R. Hamo, R. Saporta, B. A. Rosen, *ACS Appl. Energ. Mater.* **2021**, *4*, 2130–2137.

[35] P. Collini, S. Kota, A. D. Dillon, M. W. Barsoum, A. T. Fafarman, *J. Electrochem. Soc.* **2017**, *164*(9), D573–D580.

[36] J. Liu, C. Zhong, X. Du, Y. Wu, P. Xu, J. Liu, *Electrochim. Acta.* **2013**, *100*, 164–170.

[37] X. Jian, T. Li, S. Guo, L. Gao, F. Fu, Y. Tian, Y. Wu, *ACS Appl. Energ. Mater.* **2022**, *5*, 3092–3099.

[38] X. Jian, M.-M. Zhang, R. Li, J.-X. Liu, F. Fu, Z.-H. Liang, *Electrochim. Acta.* **2022**, *411*, 140091.

[39] X. Jian, T.-T. Wei, M.-M. Zhang, R. Li, J.-X. Liu, Z.-H. Liang, *J. Electrochem. Soc.* **2021**, *168*, 096504.

[40] X. Jian, T. Li, S. Guo, F. Fu, Y. Tian, B. Tian, Y. Wu, *J. Electrochem. Soc.* **2022**, *169*, 036507.

[41] S. Guo, X. Jian, X. Hou, J. Wu, B. Tian, Y. Tian, *Electrocatalysis.* **2022**, *13*, 469–478.

[42] W. Yajing, W. Jiankang, H. Guokang, D. Chunyu, D. Qihuang, G. Yunzhi, Y. Geping, S. Ying, *Ceram. Int.* **2019**, *45*, 2411–2417.

[43] B. Dai, B. Zhao, X. Xie, T. Su, B. Fan, R. Zhang, R. Yang, *J. Mater. Chem. C.* **2018**, *6*, 5690–5697.

[44] S. Anantharaj, S. Kundu, *ACS Energy Lett.* **2019**, *4*, 1260–1264.

[45] B. E. Conway, B. V. Tilak, *Electrochim. Acta.* **2002**, *47*, 3571–3594.

[46] Y. Zheng, Y. Jiao, M. Jaroniec, S. Z. Qiao, *Angew. Chem. Int. Ed.* **2015**, *54*, 52–65.

[47] C. Cui, R. Cheng, H. Zhang, C. Zhang, Y. Ma, C. Shi, B. Fan, H. Wang, X. Wang, *Adv. Funct. Mater.* **2020**, *30*, 2000693.

[48] Z. Jiangjiang, W. Erqing, C. Shiqiang, Y. Shubin, Z. Xiaolong, G. Yongji, *Nano Lett.* **2022**, *22*, 1398–1405.

[49] C. E. Park, G. H. Jeong, J. Teerthagiri, H. Lee, M. Y. Choi, *ACS Nano* **2023**, *17*, 7539–7549.

[50] K. Wei, L. Lihong, Y. Xiaoxia, X. Zhongyuan, C. Yawei, T. Muhammad, L. Zehua, D. Jinxia, S. Yanlin, *Nano Res.* **2023**. *16*, 195–201.

Manuscript received: June 25, 2024
Revised manuscript received: July 30, 2024
Accepted manuscript online: July 31, 2024
Version of record online: ■■, ■■

RESEARCH ARTICLE

Pulse-electrodeposition was used to deposit Platinum (Pt) nanostructures on $Ti_3C_2T_z$ MXene which was previously electrophoretically deposited on gas diffusion layer (GDL). The Pt morphology and loading were controlled by changing t_{on} and cycle number using a constant duty cycle (θ) of 50 %. As-synthesized catalysts were active towards hydrogen evolution reaction (HER). The catalyst with the lowest Pt loading (MX_Pt-15-5) outperformed commercial Pt/C interms of mass activity.

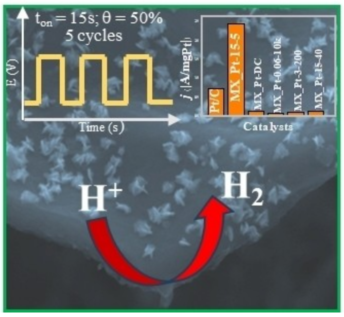

S. Chakrabartty, H. Parse, M. Krämer, S.-H. Kim, D. Raabe, B. Gault, M. Sokol, B. A. Rosen, N. Eliaz**

1 – 9

$Ti_3C_2T_z$ Supported Pulse-Electrodeposited Pt Nanostructures for Enhanced Acidic Electrochemical Hydrogen Evolution